Scuola di Dottorato in Ingegneria Leonardo da Vinci – a.a. 2009/10

PROPRIETÀ MECCANICHE, OTTICHE, ELETTRONICHE DEI MATERIALI ALLE PICCOLE E PICCOLISSIME SCALE

Versione 1 – Settembre 2010 – http://www.df.unipi.it/~fuso/dida

Parte 5
Misura di proprietà meccaniche alla nanoscala e alcuni fenomeni meccanici su scala piccola e piccolissima

Me 29.09 13-15 aula S1 DF

Outlook

- How to use force microscopy to get information on mechanical properties at the small and ultra-small scales
- Viscoelasticity and phase contrast AFM (tapping mode)
- Material hardness and nanoindentation
- Lateral force microscopy and friction coefficients at the small and ultra-small scales
- Probing mechanical properties of isolated nanostructures: the relevant example of carbin nanotubes

Phase imaging techniques

Animations at www.ntmdt.com!

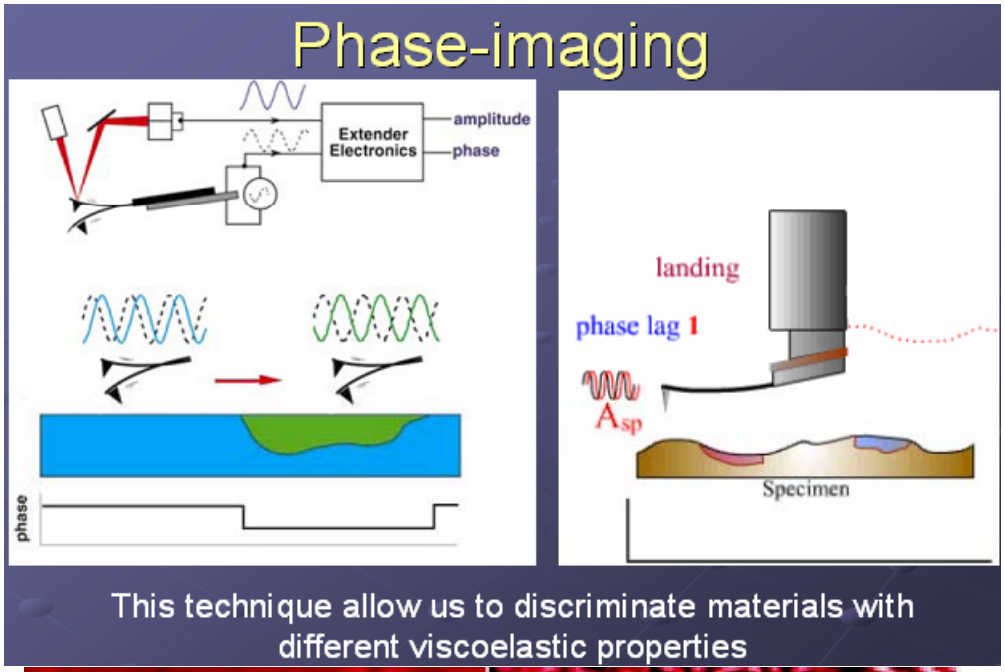

Dephasing between mechanical oscillation (e.g., the tapping oscillation) and the response of the surface (affecting the tip deflection) depends on the viscoleasticity of the surface (purely elastic vs Newton fluid)

Interpretation similar to a forced and damped mechanical oscillator

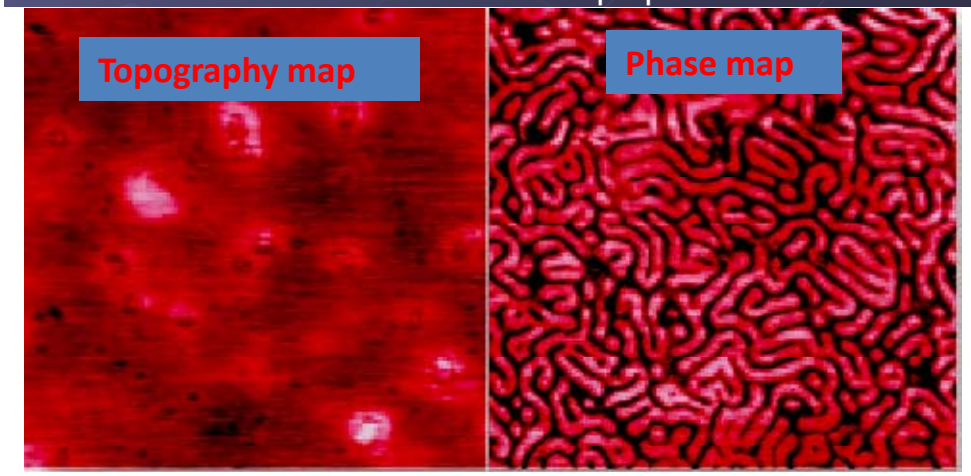

Phase imaging:
- adds a contrast mechanism;
- allows for local material analyses

An interesting mechanical property: viscoelasticity

Viscoelasticity is the property of materials that exhibit both viscous and elastic characteristics when undergoing deformation. Viscous materials, like honey, resist shear flow and strain linearly with time when a stress is applied. Elastic materials strain instantaneously when stretched and just as quickly return to their original state once the stress is removed. Viscoelastic materials have elements of both of these properties and, as such, exhibit time dependent strain. Whereas elasticity is usually the result of bond stretching along crystallographic planes in an ordered solid, viscosity is the result of the diffusion of atoms or molecules inside an amorphous material [1]

Unlike purely elastic substances, a viscoelastic substance has an elastic component and a viscous component. The viscosity of a viscoelastic substance gives the substance a strain rate dependent on time[1]. Purely elastic materials do not dissipate energy (heat) when a load is applied, then removed[1]. However, a viscoelastic substance loses energy when a load is applied, then removed. Hysteresis is observed in the stress-strain curve, with the area of the loop being equal to the energy lost during the loading cycle[1]. Since viscosity is the resistance to thermally activated plastic deformation, a viscous material will lose energy through a loading cycle. Plastic deformation results in lost energy, which is uncharacteristic of a purely elastic material's reaction to a loading cycle[1].

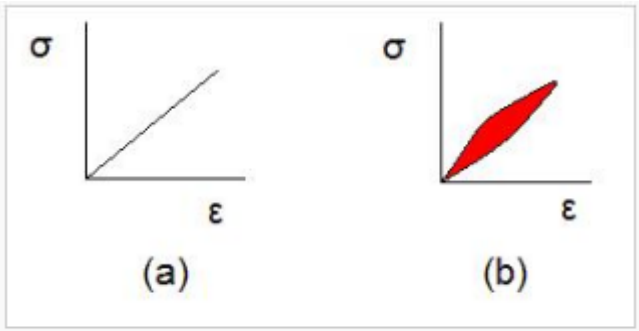

Stress-Strain Curves for a purely elastic material (a) and a viscoelastic material (b). The red area is a hysteresis loop and shows the amount of energy lost (as heat) in a loading and unloading cycle. It is equal to $\oint \sigma \, d\varepsilon$, where σ is stress and ε is strain. [1]

Specifically, viscoelasticity is a molecular rearrangement. When a stress is applied to a viscoelastic material such as a polymer, parts of the long polymer chain change position This movement or rearrangement is called Creep. Polymers remain a solid material even when these parts of their chains are rearranging in order to accompany the stress, and as this occurs, it creates a back stress in the material. When the back stress is the same magnitude as the applied stress, the material no longer creeps. When the original stress is taken away, the accumulated back stresses will cause the polymer to return to its original form. The material creeps, which gives the prefix visco-, and the material fully recovers, which gives the suffix -elasticity[2].

ne examples of viscoelastic materials include amorphous polymers, nicrystalline polymers, biopolymers, metals at very high temperatures, and nen materials. Cracking occurs when the strain is applied quickly and outside of ... elastic limit.

A **viscoelastic** material has the following properties:

- hysteresis is seen in the stress-strain curve.
- stress relaxation occurs: step constant strain causes decreasing stress
- creep occurs: step constant stress causes increasing strain

Viscoelasticity can be addressed at the local scale by using AFM in phase contrast

At the small scale, it is associated with some friction occurring in the harmonic oscillators

Origin of phase contrast I

Assuming a dynamic system is in equilibrium, the average energy input must equal the average energy output or dissipation. Applying this rule to an AFM running in a dynamic mode means that the average power fed into the cantilever oscillation by an external driver, denoted as $\bar{P}_{in}$, must equal the average power dissipated by the motion of the cantilever beam $\bar{P}_0$ and by tip–sample interaction $\bar{P}_{tip}$:

$$\bar{P}_{in} = \bar{P}_0 + \bar{P}_{tip} \qquad (1)$$

Transferred power balance

The term $\bar{P}_{tip}$ is what we are interested in, since it gives us a direct physical quantity to characterise the tip–sample interaction. Therefore we have first to calculate and then measure the two other terms in Eq. (1), in order to determine the power dissipated when the tip periodically probes the sample surface. This requires an appropriate rheological model to describe the dynamic system. Although there are investigations in which the complete flexural motion of the cantilever beam has to be considered [13], a simplified model, comprising a spring and two dashpots, represents a good approximation in this case (Fig. 1a).

The spring, characterised by the constant k according to Hooke's law, represents the only channel through which power P_{in} can be delivered to the oscillating tip $z(t)$ by the external driver $z_d(t)$. Therefore the instantaneous power fed into the dynamic system is the force exerted by the driver times the velocity of the driver: [1]

$$P_{in}(t) = F_d(t)\,\dot{z}_d(t) = k[z(t) - z_d(t)]\,\dot{z}_d(t) \qquad (2)$$

Elastic model (probe)

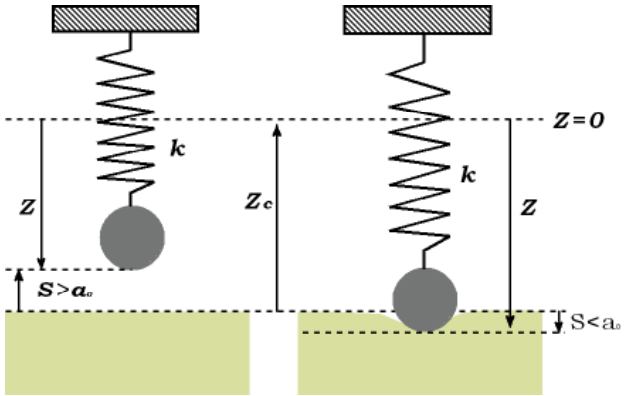

Assuming a sinusoidal steady state response and that the base of the cantilever is driven sinusoidally $z_d(t) = A_d \cos(\omega t)$ with amplitude A_d and frequency ω, the deflection from equilibrium of the end of the cantilever can be written as $z(t) = A\cos(\omega t - \varphi)$, with A and $0 \le \varphi \le \pi$ denoting the oscillation amplitude and phase shift, respectively. This allows us to calculate the average power input per oscillation cycle by integrating Eq. (2) over one period $T = 2\pi/\omega$:

$$\bar{P}_{in} = \frac{1}{T}\int_0^T P_{in}(t)\,dt = \frac{1}{2}k\omega A_d A \sin\varphi$$

Average power per cycle

Power depend on phase shift

This contains the familiar result that the maximum power is delivered to an oscillator when the response is 90° out of phase with the drive.

B. Anczykowski et al. / Applied Surface Science 140 (1999) 376–382

Origin of phase contrast II

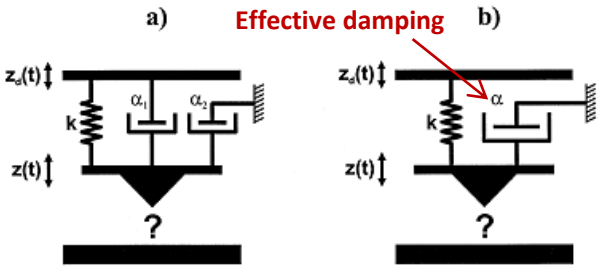

Fig. 1. Rheological models applied to describe the dynamic AFM system, comprising the oscillating cantilever and tip interacting with the sample surface. The movement of the cantilever base and the tip is denoted as $z_d(t)$ and $z(t)$, respectively. The cantilever is characterised by the spring constant k and the damping constant α. (a) In a first approach, damping is broken into two pieces α_1 and α_2: First, intrinsic damping caused by the movement of the cantilever's tip relative to its base and second, damping related to the movement of the cantilever body in a surrounding medium, e.g., air damping. (b) In first order approximation, these two contributions can be combined to one effective damping constant α. Note that *no* specific force–distance dependencies are introduced to model the actual tip-sample interaction.

The simplified rheological model as it is depicted in Fig. 1a exhibits two major contributions to the damping term $\bar{P}_0$. Both are related to the motion of the cantilever body and assumed to be well modeled by viscous damping, caused by the deflection of the cantilever beam, i.e., the motion of the tip relative to the cantilever base. Therefore the instantaneous power dissipated by such a mechanism is given by

$$P_{01}(t) = |F_{01}(t)\dot{z}(t)| = |\alpha_1[\dot{z}(t) - \dot{z}_d(t)]\dot{z}(t)| \qquad (4)$$

Power dissipated with damping

Note that the absolute value has to be calculated, since all dissipated power is 'lost' and therefore cannot be returned to the dynamic system.

However, when running an AFM in ambient conditions an additional damping mechanism has to be considered. Damping due to the motion of the cantilever body in the surrounding medium, e.g., air damping, is in most cases the dominant effect. The corresponding instantaneous power dissipation is given by

$$P_{02}(t) = |F_{02}(t)\dot{z}(t)| = \alpha_2 \dot{z}^2(t)$$

Damping by motion in a viscous environment

In order to calculate the average power dissipation, Eqs. (4) and (5) have to be integrated over one complete oscillation cycle. This yields

$$\begin{aligned}\bar{P}_{01} &= \frac{1}{T}\int_0^T P_{01}(t)\,\mathrm{d}t \\ &= \frac{1}{\pi}\alpha_1\omega^2 A\left[(A - A_d\cos\varphi)\arcsin\left(\frac{A - A_d\cos\varphi}{\sqrt{A^2 + A_d^2 - 2AA_d\cos\varphi}}\right) + A_d\sin\varphi\right]\end{aligned} \qquad (6)$$

$$\bar{P}_{02} = \frac{1}{T}\int_0^T P_{02}(t)\,\mathrm{d}t = \tfrac{1}{2}\alpha_2\omega^2 A^2 \qquad (7)$$

Considering the fact that commonly used cantilevers exhibit a quality factor of at least several hundreds (in UHV several ten thousands), we can assume that the oscillation amplitude is significantly larger than the drive amplitude when the dynamic system is driven at or near its resonance frequency: $A \gg A_d$. Therefore, Eq. (6) can be simplified in first order approximation to an expression similar to Eq. (7). Combining the two equations yields the total average power dissipated by the oscillating cantilever

$$\bar{P}_0 = \tfrac{1}{2}\alpha\omega^2 A^2 \quad \text{with } \alpha = \alpha_1 + \alpha_2 \qquad (8)$$

Dissipated power is estimated as the difference between input (driving) power and power intrinsically used by the cantilever (spring) in its oscillation

Origin of phase contrast III

We can now solve Eq. (1) for the power dissipation localised to the small interaction volume of the probing tip with the sample surface. Furthermore, by expressing the damping constant α in terms of experimentally accessible quantities such as the spring constant k, the quality factor Q_{cant} and the natural resonant frequency ω_0 of the free oscillating cantilever, $\alpha = k/(Q_{\mathrm{cant}}\omega_0)$, we obtain:

$$\bar{P}_{\mathrm{tip}} = \bar{P}_{\mathrm{in}} - \bar{P}_0 = \frac{1}{2}\frac{k\omega}{Q_{\mathrm{cant}}}\left[Q_{\mathrm{cant}} A_{\mathrm{d}} A \sin\varphi - A^2\frac{\omega}{\omega_0}\right] \tag{9}$$

Note that, so far, no assumptions have been made on how the AFM is operated, except that the motion of the oscillating cantilever has to remain sinusoidal to a good approximation. Therefore, Eq. (9) is applicable to a variety of different dynamic AFM modes.

Now let us consider another dynamic AFM mode, often referred to as tapping mode and which is commonly used in AFMs running in ambient conditions [3]. In this case the cantilever is driven at a fixed frequency and with a constant drive amplitude, while the oscillation amplitude and phase shift may change when the probing tip interacts with the sample surface. Assuming that the oscillation frequency is chosen to be ω_0, Eq. (9) can be further simplified by considering that the free oscillation amplitude A_0 is given by $A_0 = Q_{\mathrm{cant}} A_{\mathrm{d}}$. This yields

$$\bar{P}_{\mathrm{tip}} = \frac{1}{2}\frac{k\omega_0}{Q_{\mathrm{cant}}}\left[A_0 A_{\sin\varphi} - A^2\right] \tag{10}$$

Eq. (10) implies that if the oscillation amplitude A is kept constant by a feedback loop, like it is commonly done in tapping mode, simultaneously acquired phase data can be interpreted in terms of energy dissipation. When analysing such phase images [14–16], one has also to consider the fact that the phase may also change due to the transition from net attractive ($\varphi > 90°$) to net repulsive ($\varphi < 90°$) interaction between the tip and the sample [17,18]. More details on how to interpret phase data are discussed in Ref. [12].

Dissipated power depends on the phase shift (and viceversa!)

Phase shift and approach

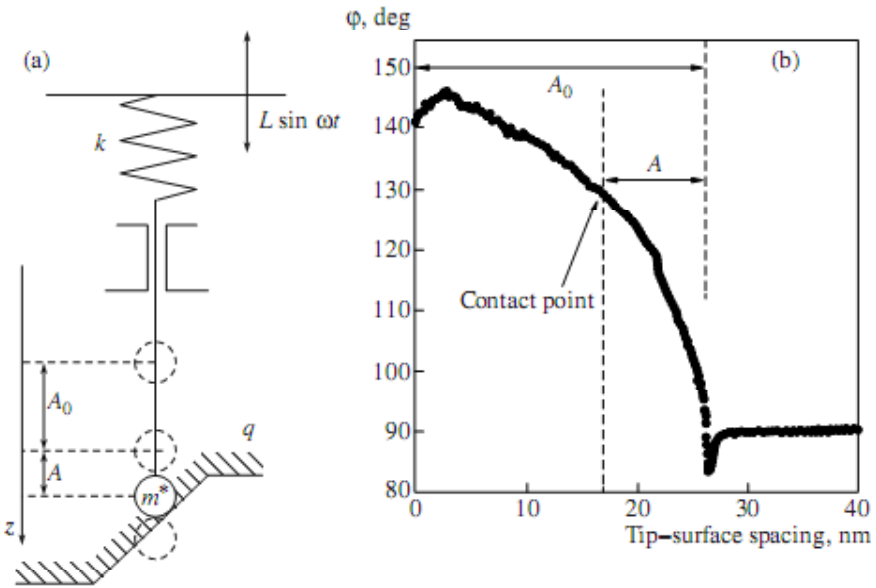

Fig. 1. (a) Schematic diagram illustrating the interaction of the tip with the surface in the model of an oscillator with a constraining force and friction. (b) Dependence of the phase shift of the oscillating cantilever on the distance between the tip and the surface.

$$\sin\varphi = \frac{A\omega}{A_0\omega_0} + \frac{QE_{diss}}{AA_0k\pi}, \qquad (2)$$

where A_0 and ω_0 are the amplitude and frequency of free oscillations of the tip, A and ω are the amplitude and frequency detected when the tip is brought to the surface, and Q is the Q factor of the cantilever.

Figure 1b demonstrates the typical experimental dependence of the normal phase shift in oscillations of the AFM cantilever on the tip-surface spacing A. The value of the normal phase shift is used to determine kinetic energy dissipation E_{diss} in each cycle of AFM tip oscillations; for this purpose, the amplitude of free tip oscillations and its distance from the surface must be fixed.

For example, in the typical case, the amplitude of free oscillations of the cantilever was $A_0 = 27.5$ nm at a frequency of tip oscillations of 156 kHz. The maximal phase shift was 57° at a distance $A_0 - A = 3.5$ nm from the surface (relative clamping $(A_0 - A)/A_0 = 0.9$). It should be noted that in the case of strong clamping, the force of interaction between the tip and the surface increases, which causes irreversible changes in the surface as well as in the tip [16]. In the case of a weak clamping between the tip and the surface, the phase shift in oscillations is sensitive to small deviations in clamping, which hampers the phase shift measurements. For this reason, we chose an intermediate amplitude $A = 10$ nm for phase shift recording (relative clamping $(A_0 - A)/A_0 = 0.6$), for which the phase shift is 38°.

URNAL OF EXPERIMENTAL AND THEORETICAL PHYSICS Vol. 106 No. 2 2008

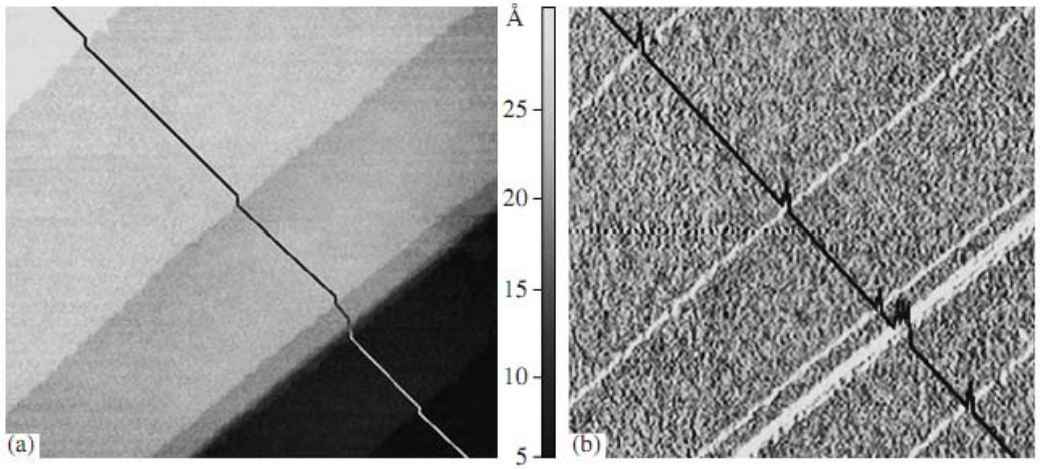

Fig. 2. Typical (a) topographic and (b) phase 5 × 5 μm AFM image of the Si(111) step surface: diagonal curves show the profiles of (a) relief and (b) phase shift.

Example of dissipation energy measurements

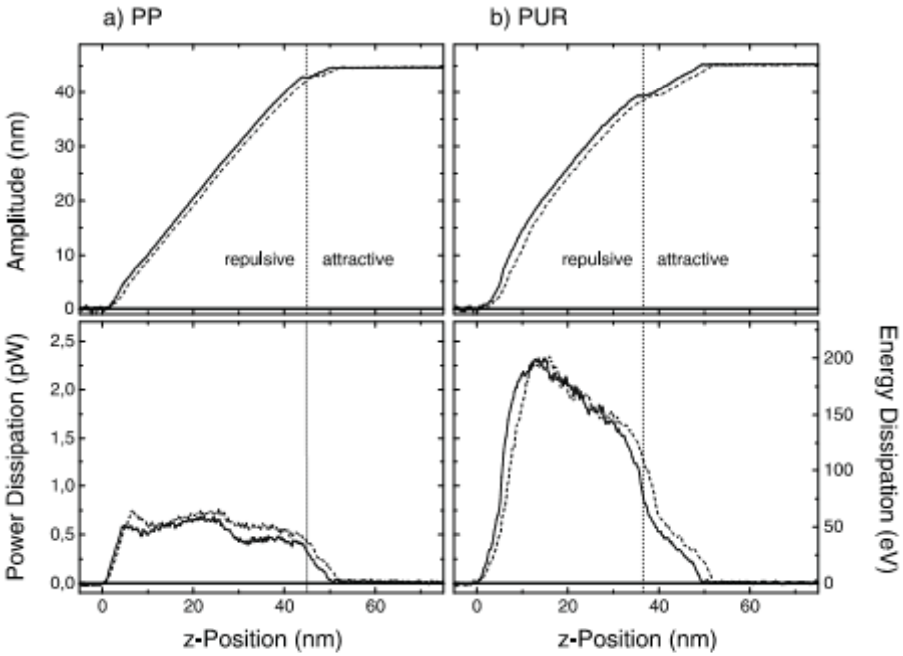

Fig. 4. Oscillation amplitude and power/energy dissipation simultaneously measured as the sample surface was approached (solid lines) and retracted (dashed lines). The small jump in the amplitude signal marks the transition point from the net attractive to the repulsive interaction regime.

Sample consists of polypropylene (PP) balls immersed in polyurethane (PUR) matrix

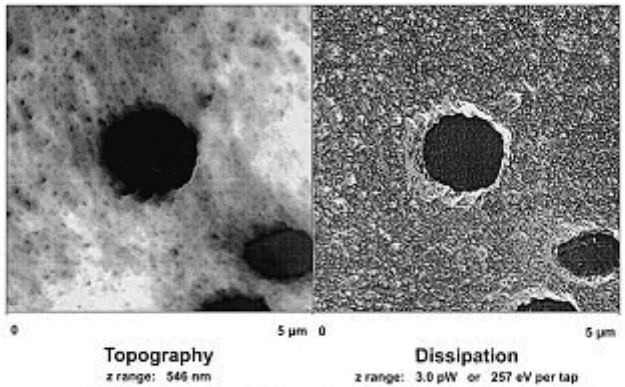

3. AFM image of a cross-section of a polymer blend: Polypropylene (PP) particles embedded in a polyurethane (PUR) matrix. The ipation image was simultaneously acquired while scanning the surface topography and exhibits a strong material contrast: Energy ipation is significantly lower on PP than on PUR.

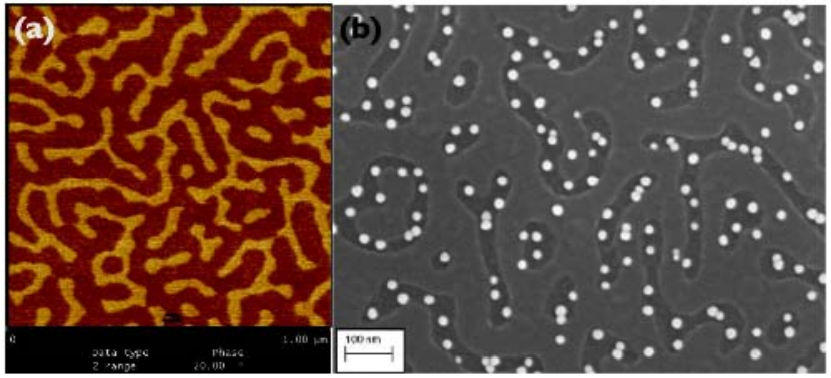

Figure 2. (a) AFM phase contrast image of PMMA-PS template. (b) SEM image of gold nanoparticles selectively bonded to the PMMA regions of the diblock copolymer template by surface chemistry techniques.

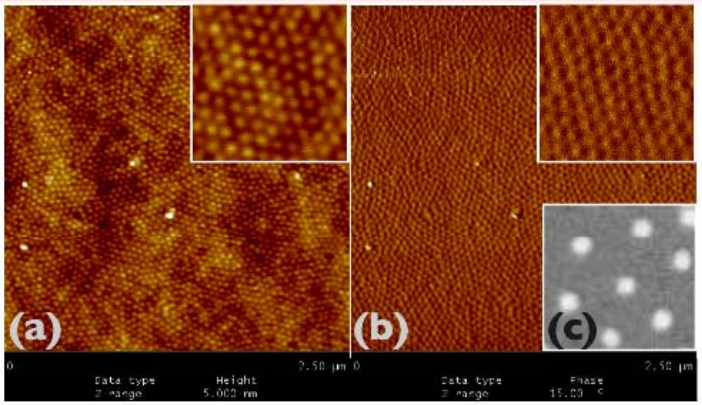

Figure 1. AFM image [(a) topography and (b) phase contrast] of PS-b-PMMA on a PS-r-PMMA/Si surface produces hexagonally packed cylindrical PMMA domains. Phase contrast images show brighter areas in the PMMA regions where elastic modulus is greater. (c) SEM image of Au nanoparticles selectively attached to hexagonal PMMA regions of the diblock copolymer array.

http://ragan-group.eng.uci.edu/diblock.html

Another interesting mechanical property: hardness

Indentation hardness tests are used to determine the hardness of a material to deformation. Several such tests exist, wherein the examined material is indented until an impression is formed; these tests can be performed on a macroscopic or microscopic scale.

When testing metals, indentation hardness correlates linearly with tensile strength. This important relation permits economically important nondestructive testing of bulk metal deliveries with lightweight, even portable equipment, such as hand-held Rockwell hardness testers. [1]

Hardness measurements quantify the resistance of a material to plastic deformation. Indentation hardness tests compose the majority of processes used to determine material hardness, and can be divided into two classes: *microindentation* and *macroindentation* tests. Microindentation tests typically have forces less than 2 N (0.45 lb_f). Hardness, however, cannot be considered to be a fundamental material property. Instead, it represents an arbitrary quantity used to provide a relative idea of material properties.[2] As such, hardness can only offer a comparative idea of the material's resistance to plastic deformation since different hardness techniques have different scales.

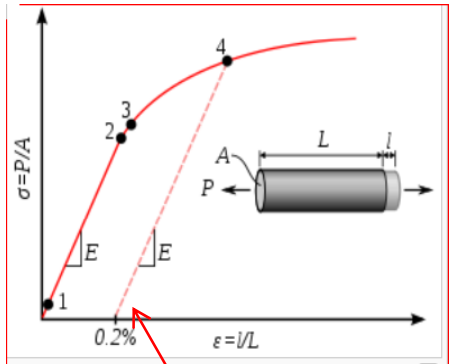

Stress-strain curve showing typical yield behavior for nonferrous alloys. Stress (σ) is shown as a function of strain (ε)

1: True elastic limit
2: Proportionality limit
3: Elastic limit
4: Offset yield strength

Plastic Offset

Macroindentation tests [edit]

The term "macroindentation" is applied to tests with a larger test load, such as 1 kgf or more. There are various macroindentation tests, including:

- Vickers hardness test (HV), which has one of the widest scales
- Brinell hardness test (HB)
- Knoop hardness test (HK), for measurement over small areas
- Janka hardness test, for wood
- Meyer hardness test
- Rockwell hardness test (HR), principally used in the USA
- Shore durometer hardness, used for polymers
- Barcol hardness test, for composite materials

There is, in general, no simple relationship between the results of different hardness tests. Though there are practical conversion tables for hard steels, for example, some materials show qualitatively different behaviors under the various measurement methods. The Vickers and Brinell hardness scales correlate well over a wide range, however, with Brinell only producing overestimated values at high loads.

Microindentation tests [edit]

The term "microhardness" has been widely employed in the literature to describe the hardness testing of materials with low applied loads. A more precise term is "microindentation hardness testing." In microindentation hardness testing, a diamond indenter of specific geometry is impressed into the surface of the test specimen using a known applied force (commonly called a "load" or "test load") of 1 to 1000 gf. Microindentation tests typically have forces of 2 N (roughly 200 gf) and produce indentations of about 50 μm. Due to their specificity, microhardness testing can be used to observe changes in hardness on the microscopic scale. Unfortunately, it is difficult to standardize microhardness measurements; it has been found that the microhardness of almost any material is higher than its macrohardness. Additionally, microhardness values vary with load and work-hardening effects of materials.[2] The two most commonly used microhardness tests are tests that also can be applied with heavier loads as microindentation tests:

- Vickers hardness test (HV)
- Knoop hardness test (HK)

In microindentation testing, the hardness number is based on measurements made of the indent formed in the surface of the test specimen. The hardness number is based on the surface area of the indent itself divided by the applied force, giving hardness units in kgf/mm². Microindentation hardness testing can be done using Vickers as well as Knoop indenters. For the Vickers test, both the diagonals are measured and the average value is used to compute the Vickers pyramid number. In the Knoop test, only the longer diagonal is measured, and the Knoop hardness is calculated based on the projected area of the indent divided by the applied force, also giving test units in kgf/mm².

Macroscopic hardness measurements

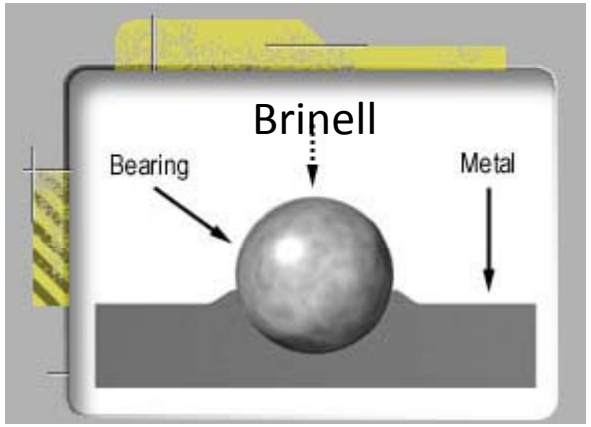

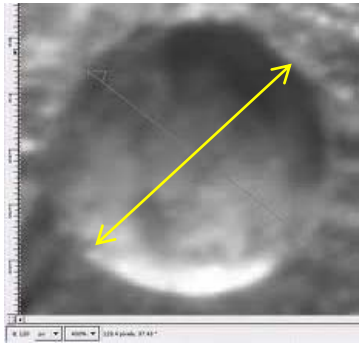

The simplest idea: to put a known load onto a surface, keep it there for some time and look at the mark left onto the surface (indentation)

Vickers

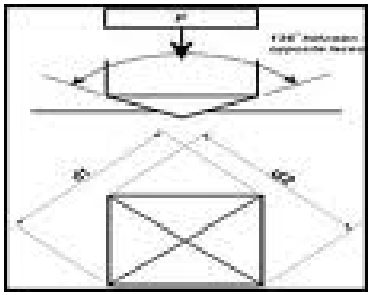

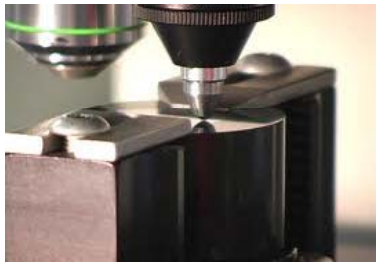

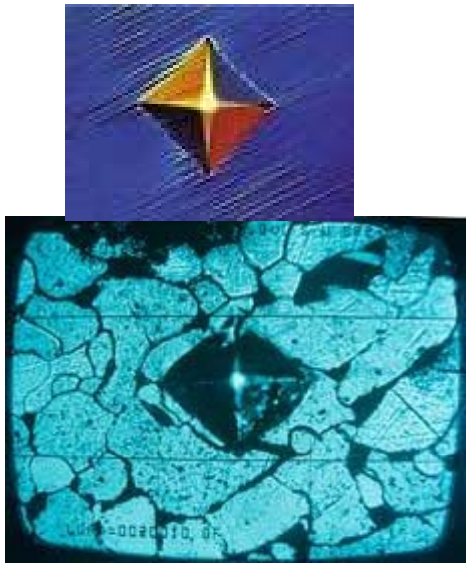

Hardness = applied load/contact area

Depth Sensing Indentation

The analysis of indentation load-penetration curves produced by depth-sensing indentation systems is often based on work by Oliver and Pharr. Their analysis was in turn based upon relationships developed by Sneddon for the penetration of a flat elastic half space by different probes with particular axisymmetric shapes (e.g., a flat-ended cylindrical punch, a paraboloid of revolution, and a cone). In general, the relationships between penetration depth, h, and load, P, for such indenter geometries can be represented in a power law expression: $P = a(h - h_f)^m$, where a contains geometric constants, the sample elastic modulus, the sample Poisson's ratio, the indenter elastic modulus, and the indenter Poisson's ratio, h_f is the final unloading depth, and m is a power law exponent that is related to the geometry of the indenter; for a flat-ended cylindrical punch, m = 1, for a paraboloid of revolution, m = 1.5, and for a cone, m = 2.

In applying this equation to the calculation of modulus, Oliver and Pharr made two significant realizations. First, the slope of the unloading curve changes constantly due to a constantly changing contact area. In prior research, the high load portion of the unloading curve was approximated as linear, which incorrectly assumes that the contact area remains constant for the initial unloading of the material. This practice created a dependence of calculated modulus values on the number of points used in the linear fit. Second, if the unloading curve can be fit by a power law expression, then a derivative, dP/dh, applied at the maximum loading point (h_{max}, P_{max}) should yield information about the state of contact at that point. This derivative was termed the contact stiffness, S, which is a function of the projected area of tip-sample contact, A, and the reduced modulus, E_r, which contains the elastic modulus (E) and Poisson's ratio (n) for both the sample and the indenter material and accounts for deformation of both the indenter and the sample.

Basic idea of DSI (after Oliver and Pharr): instead of measuring the contact area, let's measure the penentration depth upon application of a variable load

Nanoindentation and AFM

Introduction to nanoindentation

http://www.nanoindentation.cornell.edu/

Indentation tests are perhaps the most commonly applied means of testing the mechanical properties of materials. In such a test, a hard tip, typically a diamond, is pressed into the sample with a known load. After some time, the load is removed. The area of the residual indentation in the sample is measured and the hardness, H, is defined as the maximum load, P, divided by the residual indentation area, A_r , or

$H = P/A_r$

The idea of nanoindentation arose from the realization that an indentation test is an excellent way to measure very small volumes of materials. In principle, if a very sharp tip is used, the contact area between the sample and the tip, and thus the volume of material that is tested, can be made arbitrarily small. The only problem is determining the indentation area. It is easy to make an indentation that is so small that it is difficult to see without a powerful microscope.

To solve this problem depth sensing indentation methods were developed. In this method, the load and displacement of the indenter are recorded during the indentation process and these data are analyzed to obtain the contact area, and thereby mechanical properties, without having to see the indentations.

Nanoindentation refers to depth-sensing indentation testing in the submicrometer range and has been made possible by the development of 1) machines that can make such tiny indentations while recording load and displacement with very high accuracy and precision, and 2) analysis models by which the load displacement data can be interpreted to obtain hardness, modulus, and other mechanical properties.

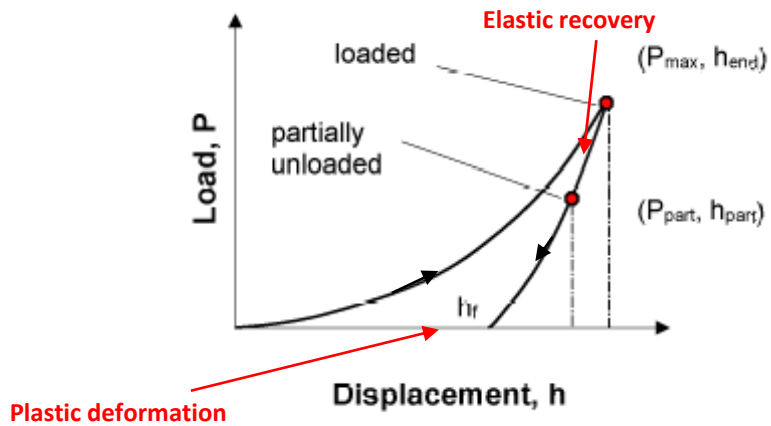

(Nano)indentation is a common technique to ascertain elastic/plastic behavior of the materials
(if carried out with a load modulation, also surface viscoelasticity can be analyzed)

Data pertaining to the elastic modulus and to the plastic behavior (e.g., shear modulus) can be attained and comparison with macroscopic results (e.g., Vickers hardness, Rockwell,…) may lead to interesting insights on the microscopic nature of surfaces and nanostructures

AFM- nanoindentation (and problems)

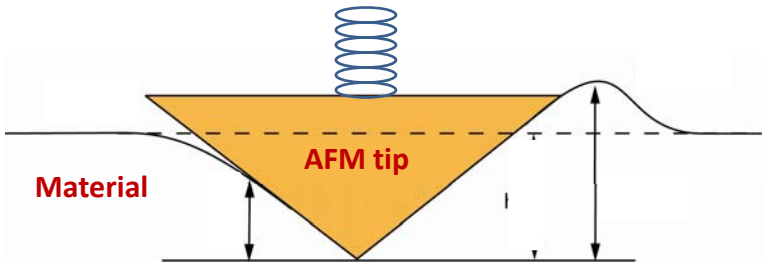

Material hardness: $H = \frac{P_{MAX}}{A_C}$

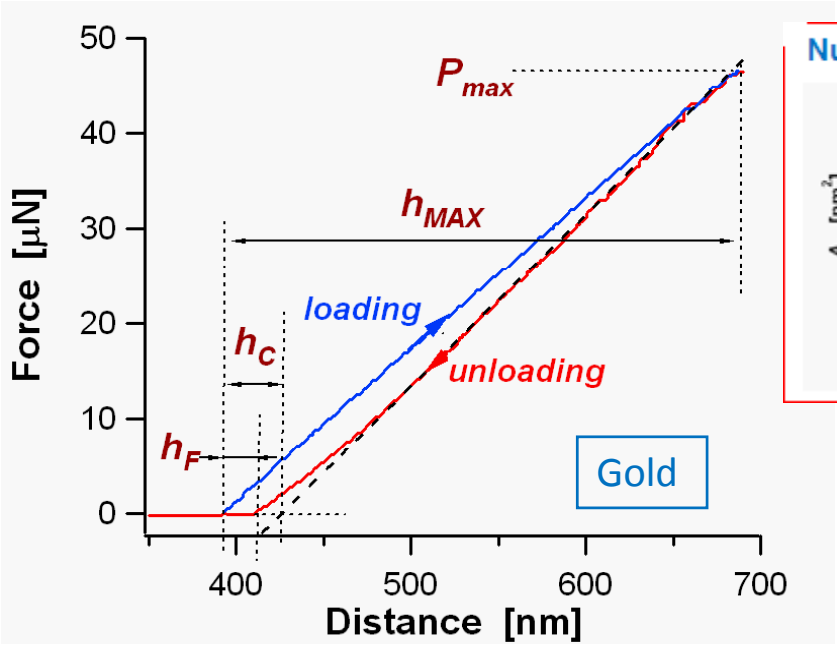

Either h_F or h_C can be used as representative of the indentation depth h

Contact area derived from *h* through specifiic models

Numerical evaluations show $A_C \propto h^m$, with m depending on the h range

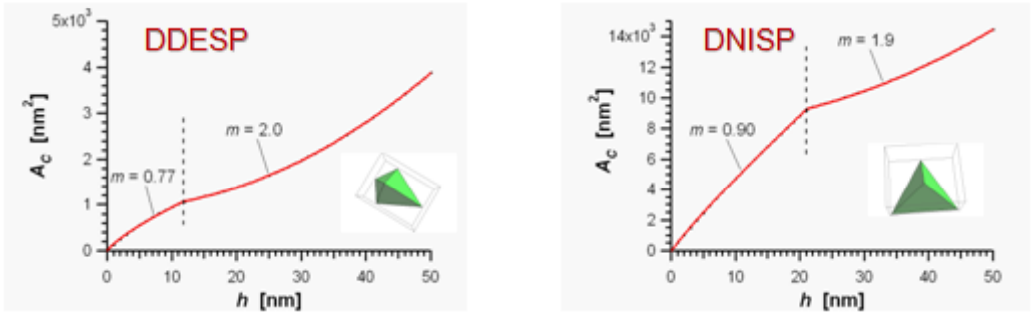

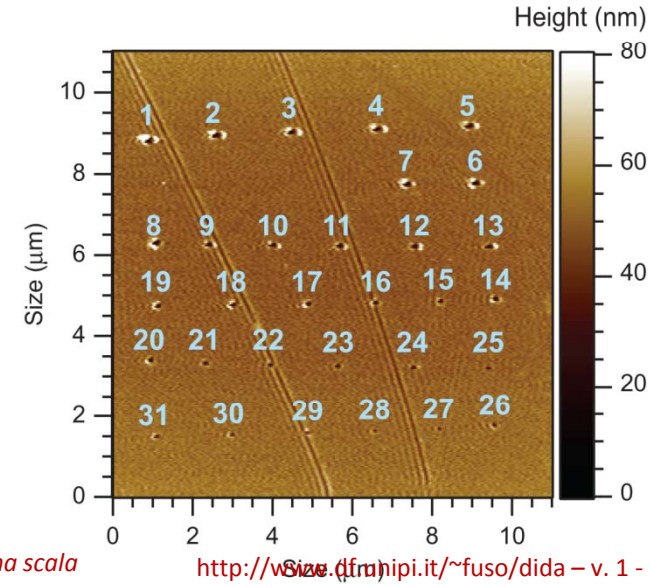

Applications of nanoindentation

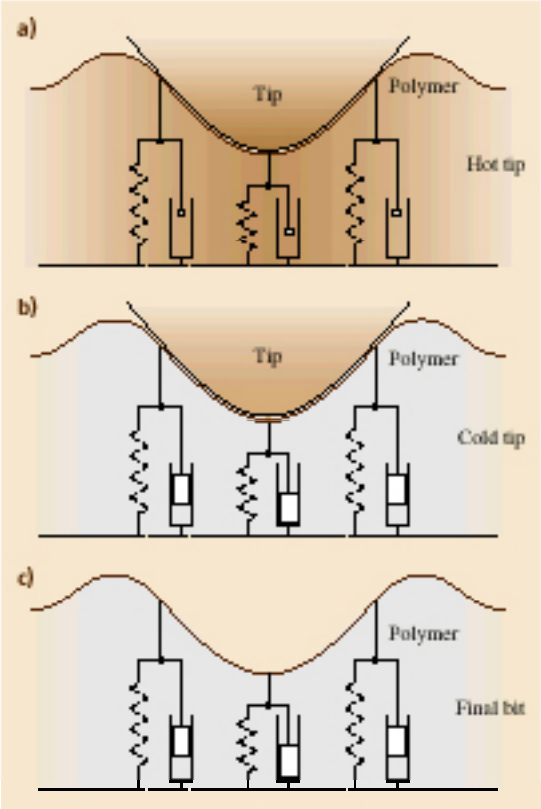

Polymers can be plastically deformed

If *thermoplastics* are used (and tip is heated), deformations can be reversed

Fig. 31.18a–c Viscoelastic model of indentation writing. (**a**) The hot tip heats a small volume of polymer material to more than Θ_g. The shear modulus of the polymer drops drastically from GPa to MPa, which in turn allows the tip to indent the polymer. In response, elastic stress (represented as compression springs) builds up in the polymer. In addition, viscous forces (represented as pistons) associated with the relaxation time for the local deformation of molecular segments limit the indentation speed. (**b**) At the end of the writing process, the temperature is quenched on a microsecond time scale to room temperature: The stressed configuration of the polymer is frozen-in (represented by the locked pistons). (**c**) The final indentation corresponds to a metastable configuration. The original unstressed flat state of the polymer can be recovered by heating the indentation volume to more than Θ_g, which unlocks the compressed springs (after [31.15])

31.7 Polymer Medium

The polymer storage medium plays a crucial role in millipede-like thermomechanical storage systems. The thin-film multilayer structure with PMMA as active layer (see Fig. 31.2) is not the only possible choice, considering the almost unlimited range of polymer materials available. The ideal medium should be easily deformable for writing, yet indentations should be stable against tip wear and thermal degradation. Finally, one would also like to be able to erase and rewrite data repeatedly. In order to be able to address all important aspects properly, some understanding of the basic physical mechanism of thermomechanical writing and erasing is required.

31.7.1 Writing Mechanism

In a *gedanken* experiment we visualize writing of an indentation as the motion of a rigid body (the tip) in a viscous medium (the polymer melt). Let us initially assume that the polymer, i. e., PMMA, behaves like a simple liquid after it has been heated above the glass-transition temperature in a small volume around the tip. As viscous drag forces must not exceed the loading force applied to the tip during indentation, we can estimate an upper bound for the viscosity ζ of the polymer melt using Stokes's equation:

$$F = 6\pi\zeta\varrho v\,. \qquad (31.1)$$

In actual indentation formation, the tip loading force is on the order of $F = 50\,\mathrm{nN}$ and the radius of curvature at the apex of the tip is typically $\varrho = 20\,\mathrm{nm}$. Assuming a depth of the indentation of, say, $h = 50\,\mathrm{nm}$ and a heat pulse of $\tau_h = 10\,\mu\mathrm{s}$ duration, the mean velocity during indentation formation is on the order of $v = h/\tau_h = 5\,\mathrm{mm/s}$. Note that thermal relaxation times are on the order of microseconds [31.20, 21] and, hence, the heating time can be equated to the time it takes to form an indentation. With these parameters we obtain $\zeta < 25\,\mathrm{Pa\,s}$, whereas typical values for the shear viscosity of PMMA are at least seven orders of magnitude larger even at temperatures well above the glass-transition point [31.39].

This apparent contradiction can be resolved by considering that polymer properties are strongly dependent on the time scale of observation. At time scales on the order of 1 ms and below, entanglement motion is in effect frozen in and the PMMA molecules form a relatively static network. Deformation of the PMMA now proceeds by means of uncorrelated deformations of short molecular segments, rather than by a flow mechanism involving the coordinated motion of entire molecular chains. The price one has to pay is that elastic stress builds up in the molecular network as a result of the deformation (the polymer is in a so-called rubbery state). On the other hand, corresponding relaxation times are orders of magnitude smaller, giving rise to an effective viscosity at millipede time scales on the order of $10\,\mathrm{Pa\,s}$ [31.39], as required by our simple argument (see (31.1)). Note that, unlike normal viscosity, this high-frequency viscosity is basically independent of the detailed molecular structure of the PMMA, i. e., chain length, tacticity, polydispersity, etc. In fact, we can even expect that similar high-frequency viscous properties can be found in a large class of other polymer materials, which makes thermomechanical writing a rather robust process in terms of material selection.

Examples of nanoindentation

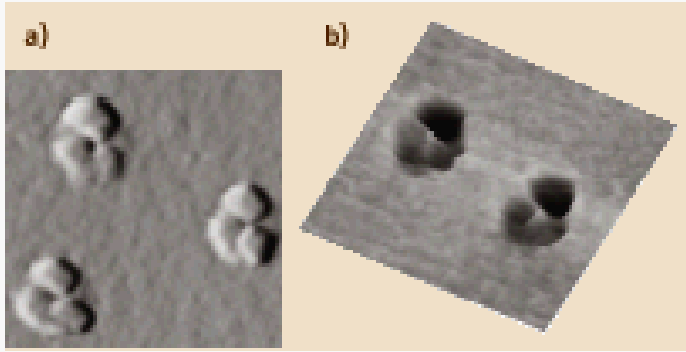

Fig. 31.20a,b Topographic image of individual indentations. (a) The region around the actual indentations clearly shows the threefold symmetry of the tip, here a three-sided pyramid. (b) The indentations themselves exhibit sharp edges, as can be seen from the inverted 3-D image. Image size is $2 \times 2\,\mu m^2$ (from [31.15] © 2002 IEEE)

Besides tribological and nanomechanical applications, nanoindentation can be envisioned as a nanofabrication tool or a data storage method

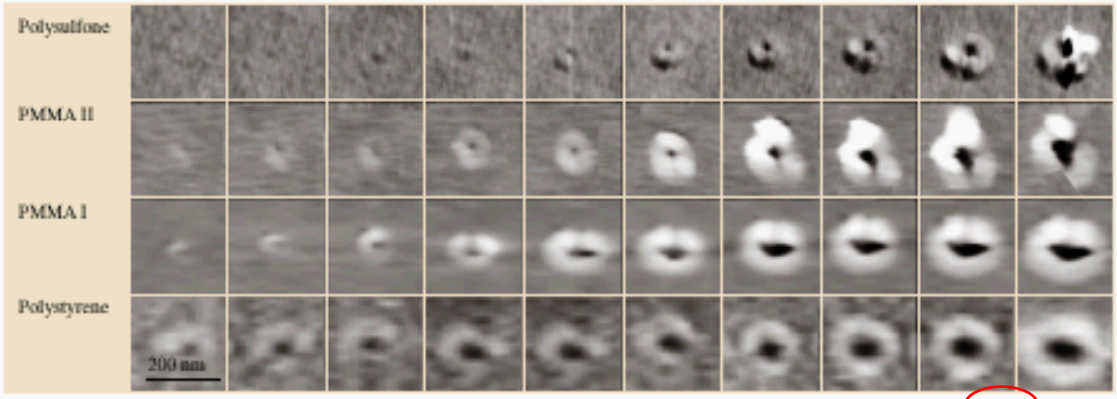

Fig. 31.21 Written indentations for different polymer materials. The heating pulse length was 10 µs, the load about 10 nN. The grey scale is the same for all images. The heater temperatures for the indentation on the left-hand side are 445, 400, 365, and 275 °C for the polymers Polysulfone, PMMA II (anionically polymerized PMMA, $M \approx 26$ k), PMMA I (Polymer Standard Service, Germany, $M \approx 500$ k), and Polystyrene, respectively. The temperature increase between events on the horizontal axis is 14, 22, 20, and 9 °C, respectively (from [31.15] © 2002 IEEE)

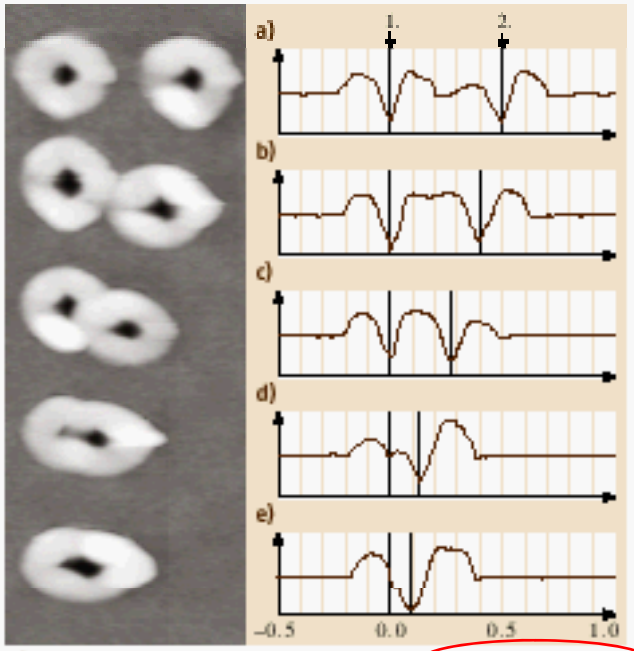

Fig. 31.24a–e Indentations in a PMMA film at several distances. The depth of the indentations is ~ 15 nm, roughly the same as the thickness of the PMMA layer. The indentations on the left-hand side were written first, then a second series of indentations was made with decreasing distance from the first series going from (a) to (e) (after [31.15])

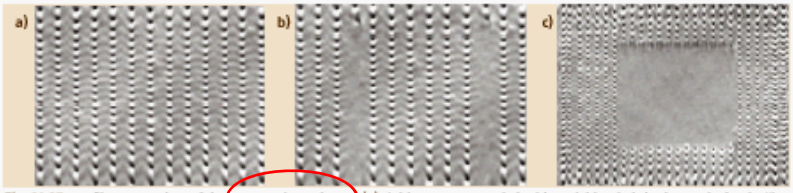

Fig. 31.25a–c Demonstration of the new erasing scheme. (a) A bit pattern recorded with variable pitch in the vertical axis (fast scan axis) and constant pitch in the horizontal direction (slow scan axis) was prepared. (b) Then two of the lines were erased by decreasing the pitch in the vertical direction by a factor of three, showing that the erasing scheme works for individual lines. One can also erase entire fields of indentations without destroying indentations at the edges of the fields. This is demonstrated in (c), where a field has been erased from an indentation field similar to the one shown in (a). The distance between the lines is 70 nm (from [31.15] © 2002 IEEE)

Da B. Bhushan, Handbook of nanotechnology (Springer, 2003)

Size effects in nanoindentation

Nanoindentation of a hard coating (BALINIT C)

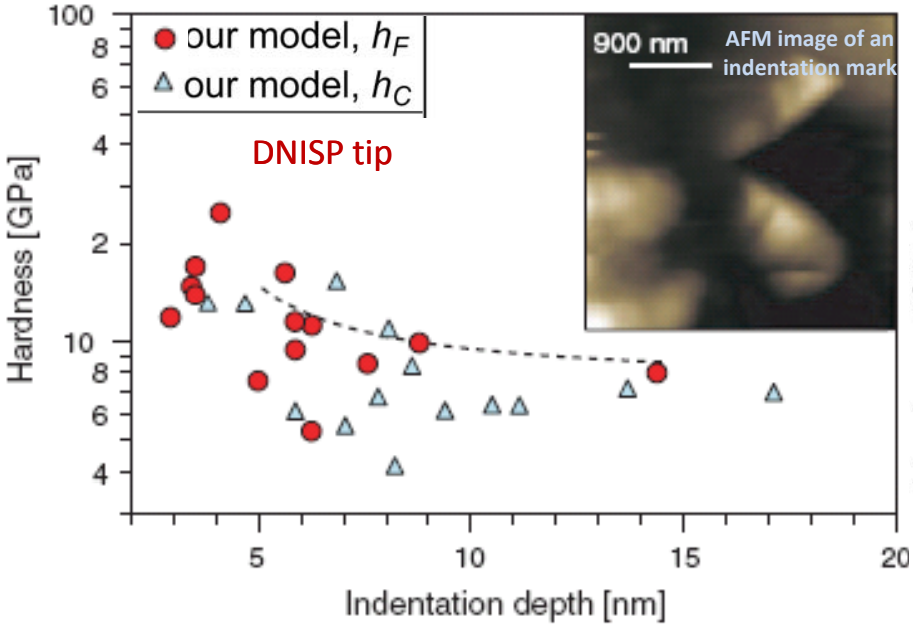

(a)	Aluminium	Bulk	DNISP
(b)	Silicon	Wafer	DNISP
(c)	Polystyrene	Layer	DDESP
(d)	PMMA	Layer	DDESP

Layers are 100 nm thick spin coated films on glass

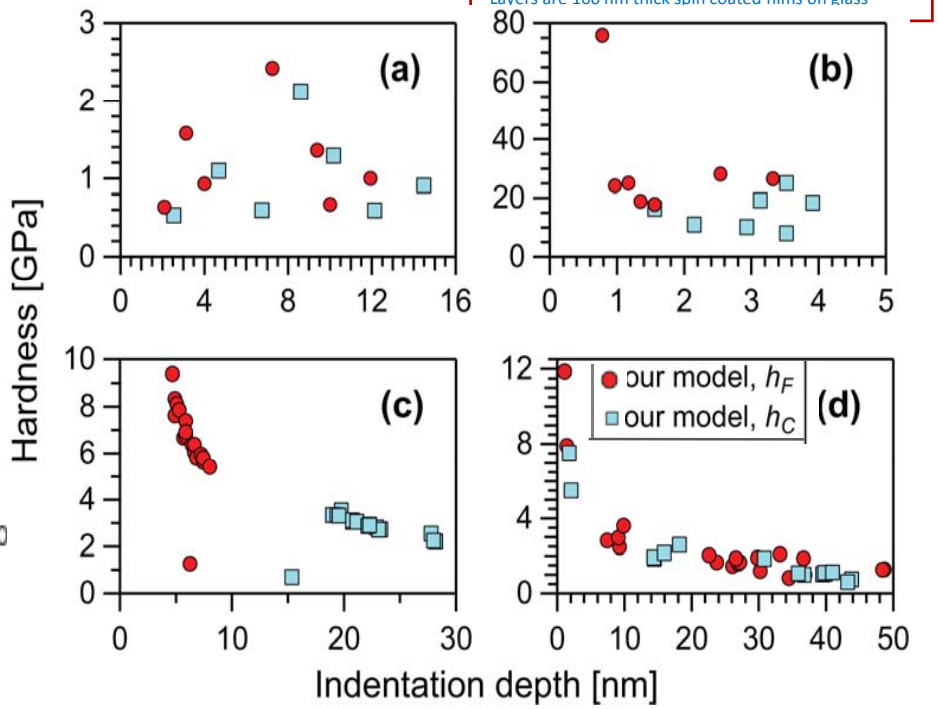

Material	Investigated depth range [nm]	α	H_0 [GPa]	Literature data [GPa]
Silicon	0.5-4.0	-1.9	13±2.4	13
Gold	5-28	-1.3	1.3±0.2	1.1-1.4
Balinit C	2-15	-1.0	5.5±1.2	5-8 (?)
Polystyrene	3.0-10	-1.2	0.83±0.22	~0.3
PMMA	1.0-30	-0.73	0.58±0.16	~0.4

Behavior of H on h_F:

$$H(h_F) = k h_F^{\alpha} + H_0$$

with k constant, $\alpha < 0$, H_0 asymptotic hardness at macroscopic indentations

(Apparent) hardness increases at small (<10 nm) indentation depths possibly due to cumbersome material accommodation at the ultra-small scale

Not to forget: adhesion forces

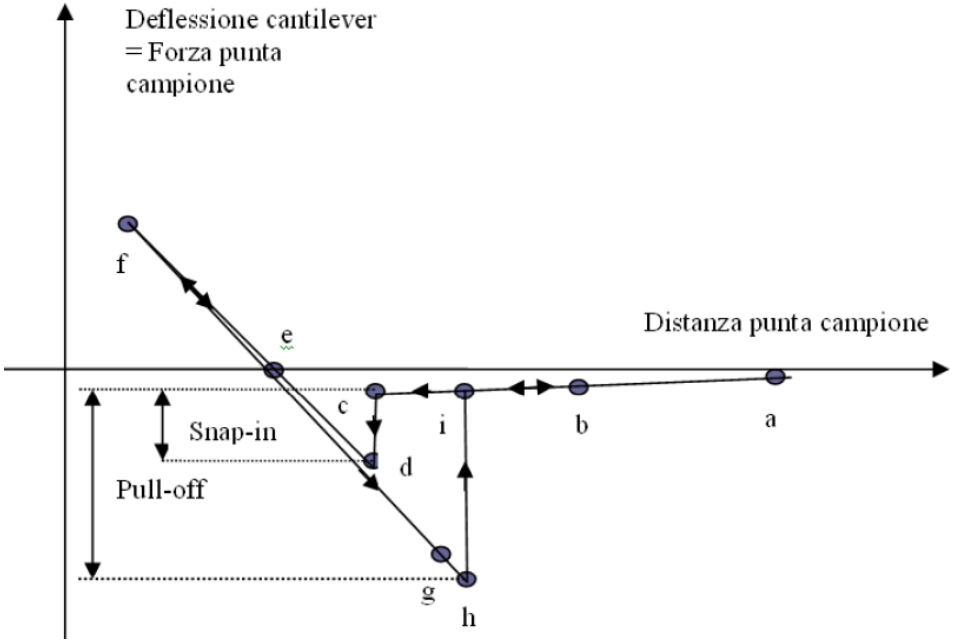

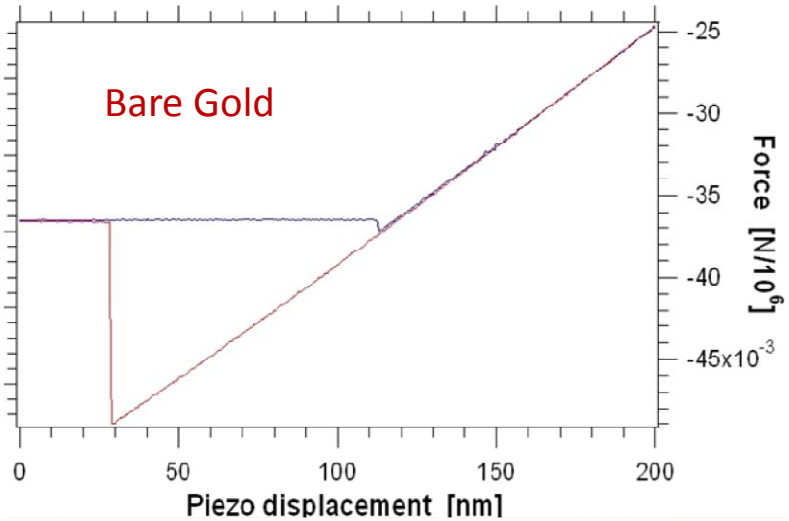

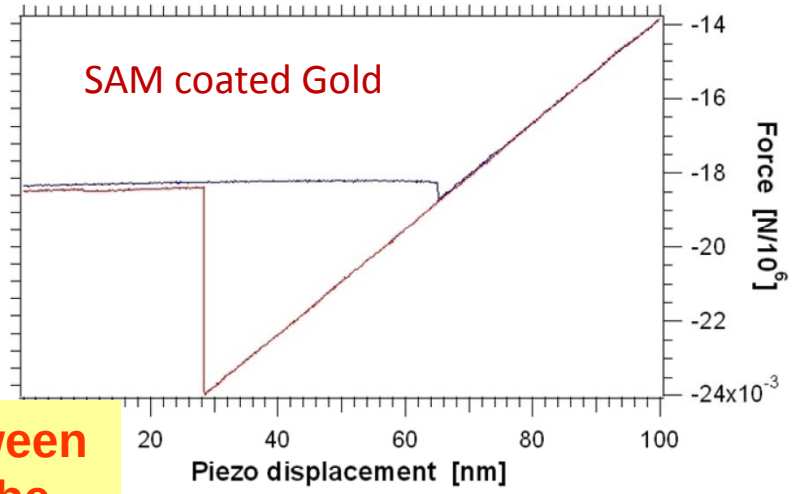

Oro: adesione = (19 ± 1) nN

SAM: adesione = (5.5 ± 0.3) nN

SAM < ORO perché ha superficie idrofobica

Lavoro adesione SAM per unità di superficie = 44 mJ/m^2

Molecola SAM = piccola molla

k molecola = 3 N/m

Adhesion forces of SAM (nonanethiol) layers

Adhesion forces between tip and surface can be accurately measured

F. Prescimone, Tesi di laurea in Scienza dei Materiali, 2008

Additional variants of force microscopy

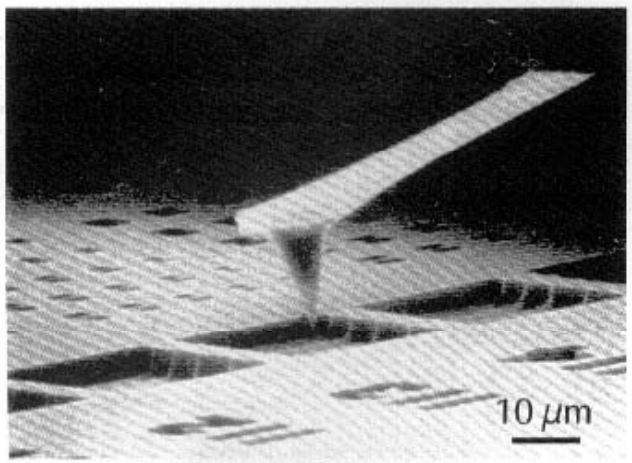

Figure 19: Scanning electron micrograph of a cantilever made of Si. [24].

We have seen how AFM, based on the occurrence of tip/surface van der Waals forces, can map the local topography of the sample

No sample preparation is needed, and the topography map is obtained with "absolute" calibration

The achievable space resolution can reach the **atomic level**, even though most common instruments are capable of a slightly smaller resolution (in the nm range, depending also on the sample properties!)

The close vicinity between tip and surface realized in AFM opens the way for probing physical **quantities other** than the van der Waals interaction force ruling the **vertical** deflection (bending) of the cantilever

*What can be learned by measuring the **lateral** motion (torsion) of the cantilever?*

Lateral Force Microscopy (LFM, SFFM)

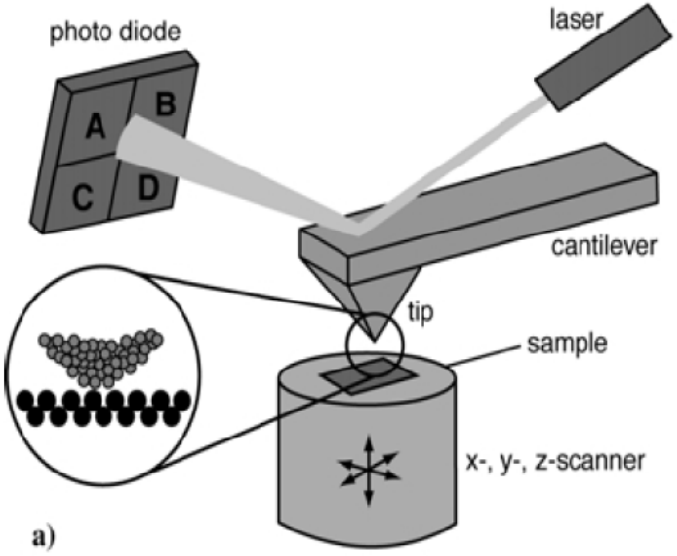

During the scan, the tip is continuously displaced with respect to the surface

Friction forces occur, resulting in a ***torsion*** of the cantilever

Cantilever torsion can be recorded by a two-dimension position sensitive detector (i.e., a 4-quadrant photodetector)

Friction effects can be corrected by the topographical artifacts by comparing forward and backward scans

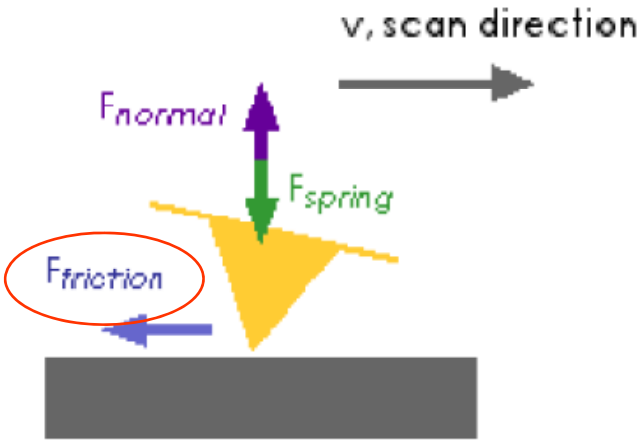

- (A+B)-(C+D) = normal force (AFM signal)
- (A+C)-(B+D) = lateral force (LFM signal)

Friction and topography: artifacts and genuine

Trace (forward scan)

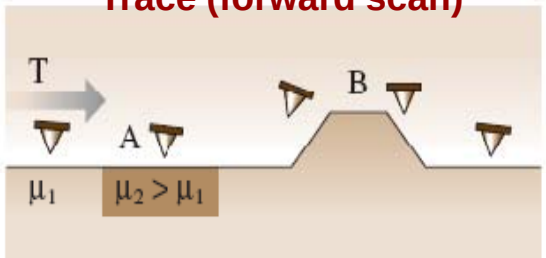

Retrace (backward scan)

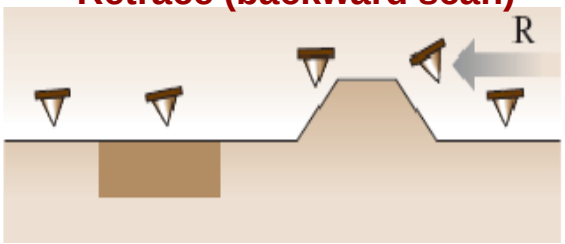

Friction force is **always** oriented against motion!

From topography data (the space derivative…)

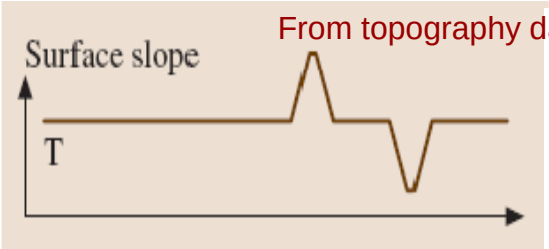

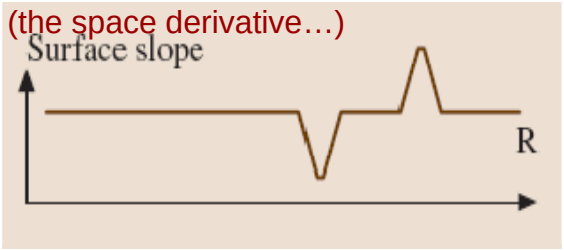

Lateral force data

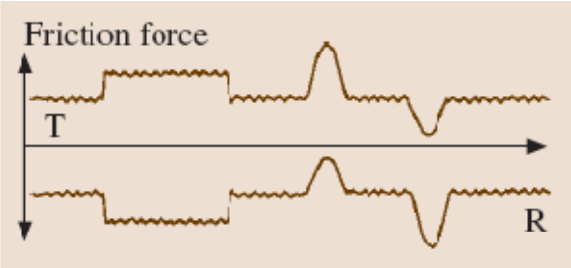

(Local) friction data

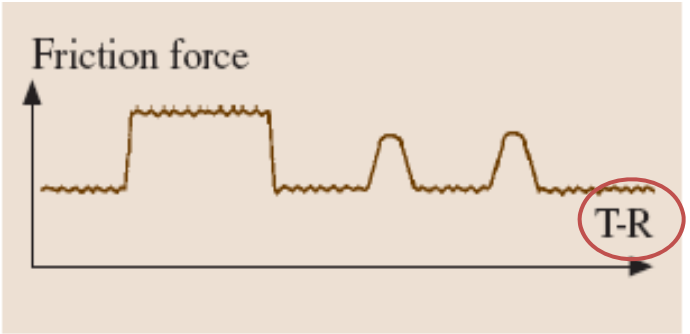

Lateral force data are always convuleted with topography (slope), but genuine information of the local friction can be derived by comparing trace and retrace and considering simultaneously acquired topography data

nanotechnology (Springer, 2003)

Examples of LFM/SFFM images

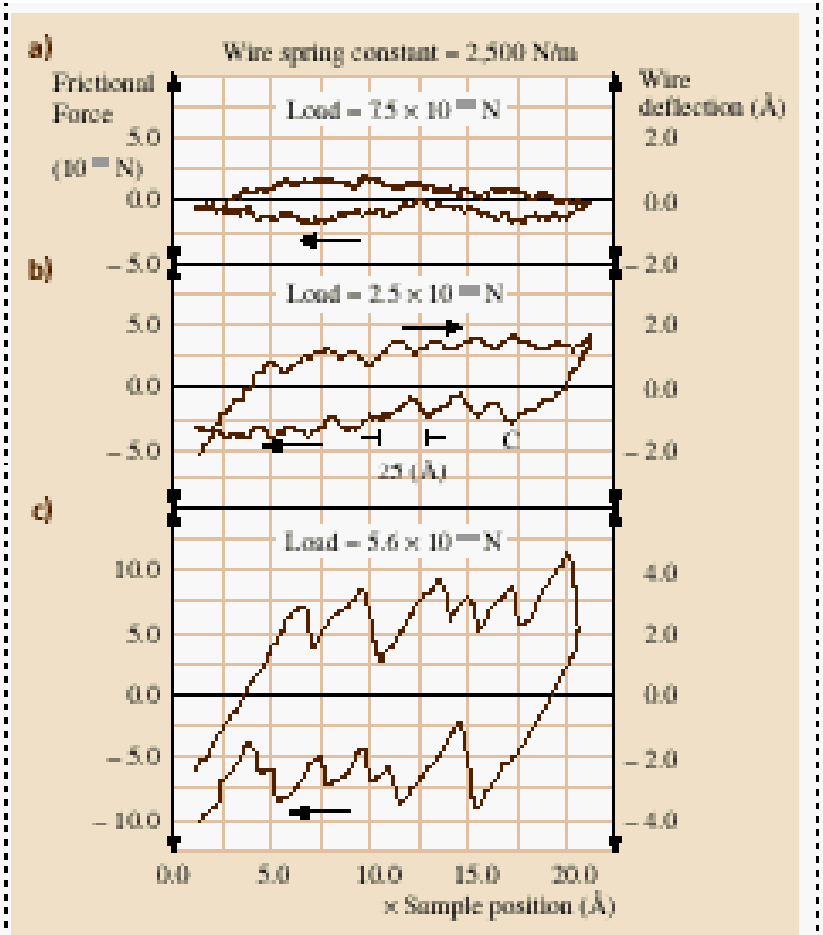

Fig. 20.15a–c Friction loops on graphite acquired with (a) F_N = 7.5 μN, (b) 24 μN and (c) 75 μN. (After [20.1])

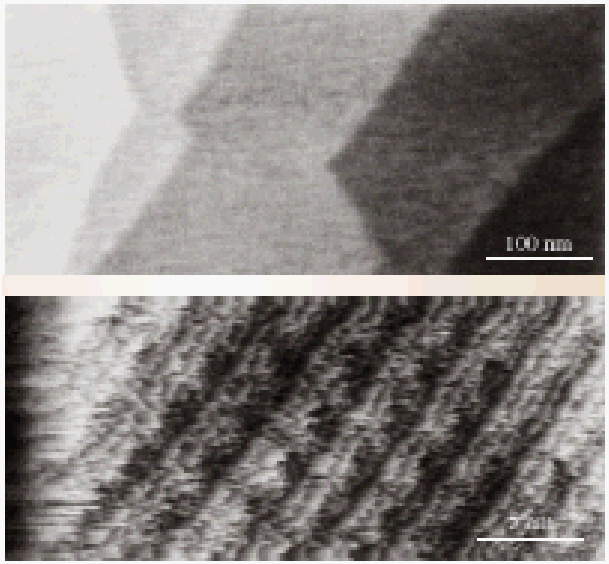

Fig. 20.18 (a) Topography and (b) friction image of Si(111)7×7 measured with a PTFE coated Si-tip. (After [20.29])

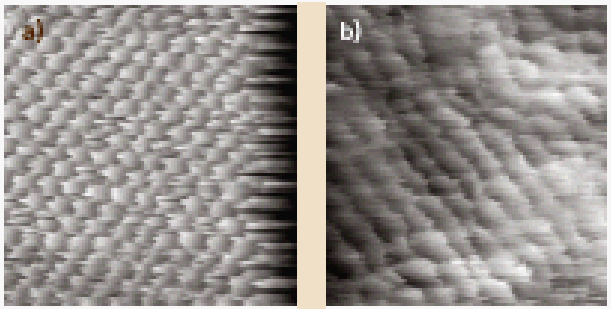

Fig. 20.19a,b Friction images of (a) Cu(111) and (b) Cu(100). Frame size: 3 nm. (After [20.34])

Da B. Bhushan, Handbook of nanotechnology (Springer, 2003)

✓**LFM/SFFM offers an additional contrast mechanism**
✓**Possibility to discriminate different materials at the atom level**
✓**Nanotribology investigations can be carried out**

A few words on nanotribology

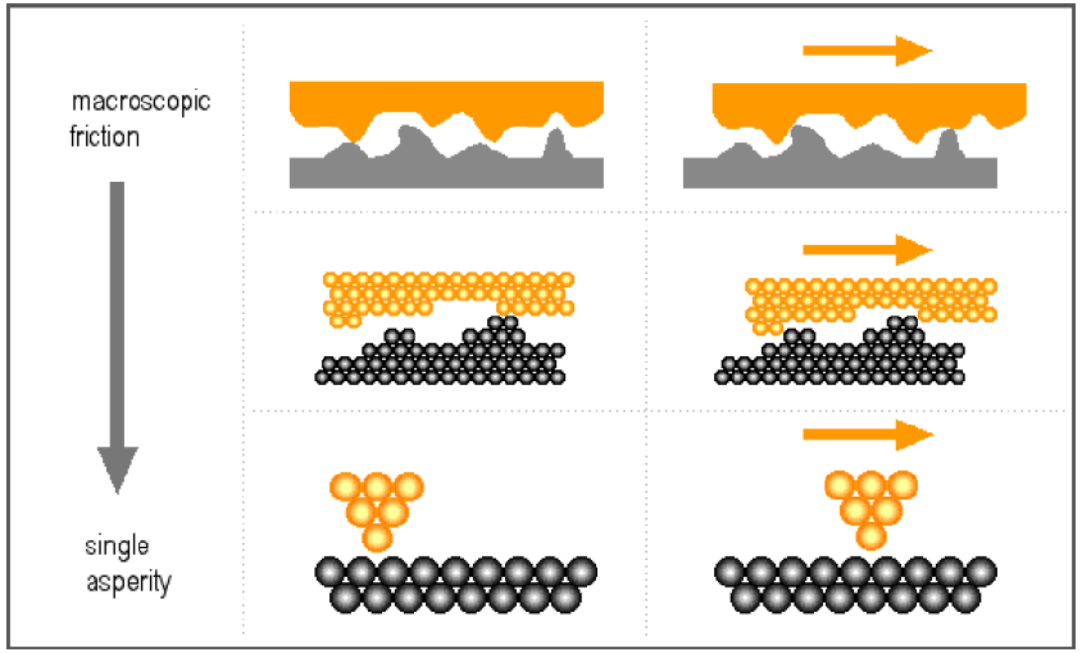

Sliding motion of the AFM tip "in contact" with the surface turns out affected by "tribological mechanisms" at the atomic scale:
- **Adhesion;**
- **Ploughing;**
- **Deformation**

- Modello di Tomlinson (1929) :

modello di attrito applicabile su scala atomica

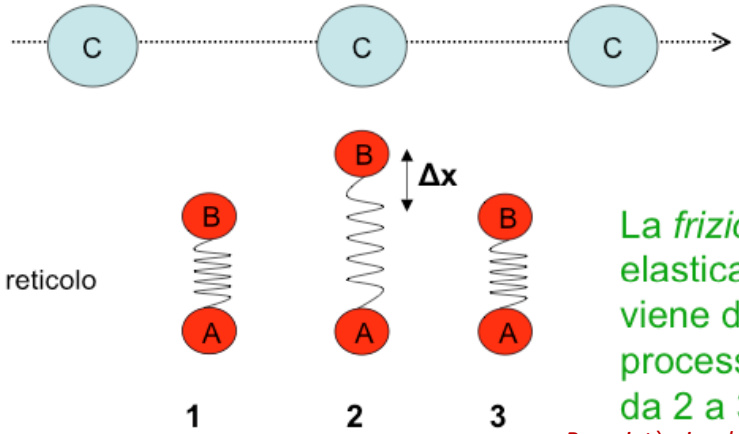

Friction models at the ultra-small scale must account for local tip /surface interaction

La *frizione* è l'energia elastica ½ $K(\Delta x)^2$ che viene dissipata nel processo di rilassamento da 2 a 3

Stick-slip mechanisms during the scan

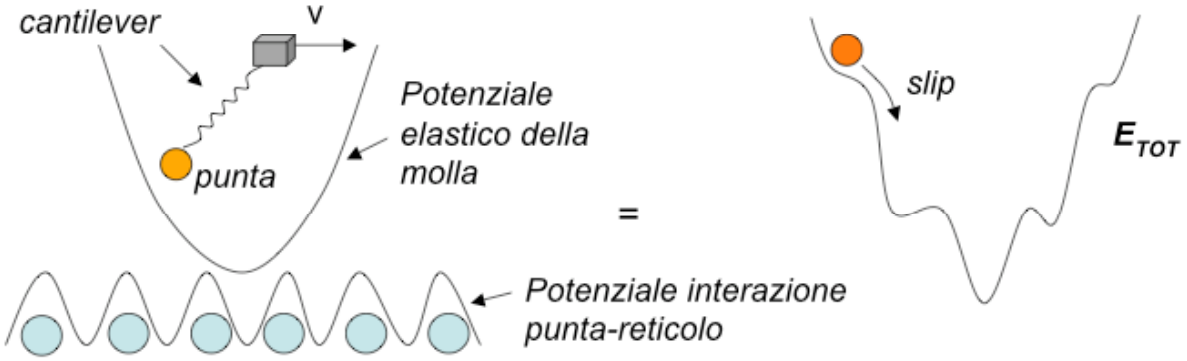

Interaction potential accounts for the periodic surface potential

Pendenza nella regione di equilibrio: costante elastica che rappresenta le interazioni punta-campione

$1/K_{eff}=1/K_T+1/K_C$

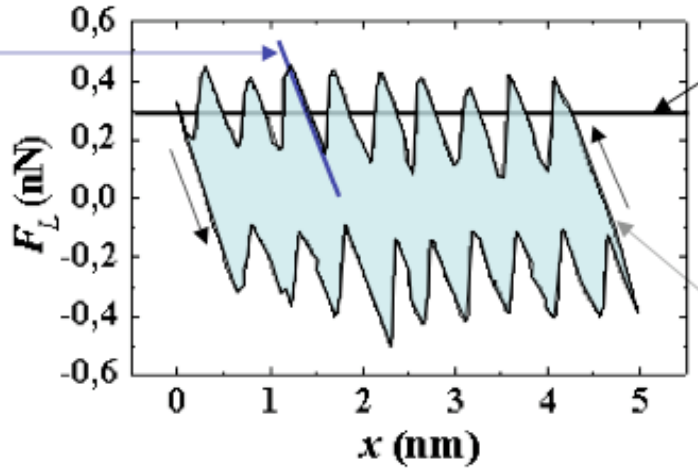

Forza laterale media: permette il calcolo di μ

Area dentro il ciclo di isteresi: energia totale dissipata

Singola linea di scansione *LFM* di NaCl a v = 2.5 nm/s

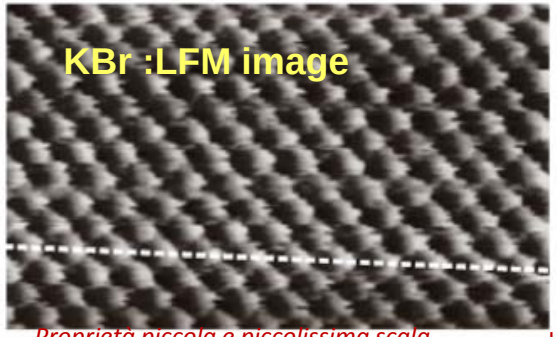

Stick and slip provide a sensitive contrast mechanism at the atomic level

AFM-based nanomechanics on isolated nanostructures

Goal: to reproduce at the ultra-small scale mecahnical analysis on macroscopic specimens (e.g, tensile or torsional stress, etc.)

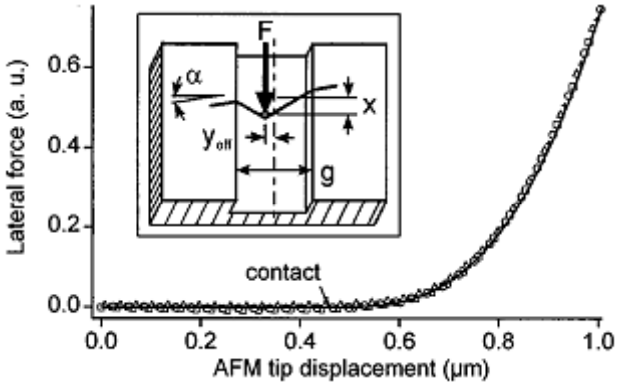

FIG. 3. (a) Lateral force on single-wall nanotube rope as a function of AFM tip position. The four symbols represent data from four consecutive lateral force curves on the same rope, showing that this rope is straining elastically with no plastic deformation. The force increases as x^3 after contact, as expected for an elastic string with no slack. The solid line is a fit of Eq. (2) to the curve marked with circles. The fit parameters correspond to elastic strain of 2.8± 0.4%. A linear background was subtracted from the data before fitting; only one in eight data points is shown for clarity. (b), inset. The AFM tip moves along the trench, in the plane of the surface, and displaces the rope as shown. Variables marked are used in Eq. (2).

TABLE I. Trench widths, angles, offsets, maximum extension of AFM tip, and observed elastic strains for four ropes tested. The dominant error in strain is due to calibration of the piezoelectric AFM scanner.

g (μm)	α (°)	y_{off} (μm)	$x_{max}-x_0$ (μm)	ϵ_{max}
4.3	0°	0.26	0.54± 0.03	2.8± 0.4%
3.7	12°	0.95	0.57±0.03	5.8± 0.9%
4.1	0°	0.67	0.31±0.02	1.2± 0.2%
4.5	0°	0.48	0.32±0.02	1.1± 0.1%

Preparation of a suitable sample si part of the research!

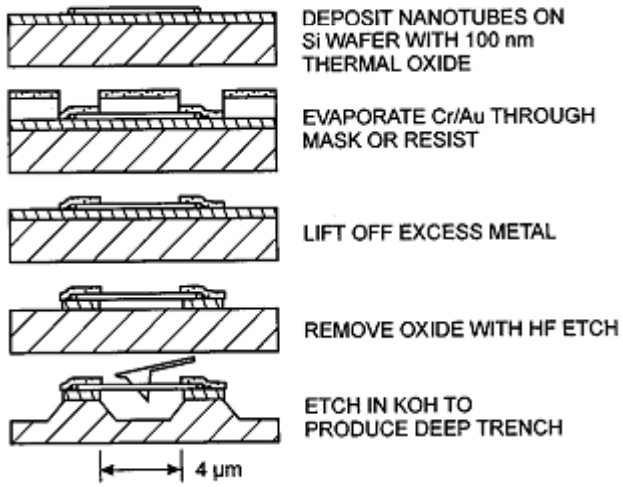

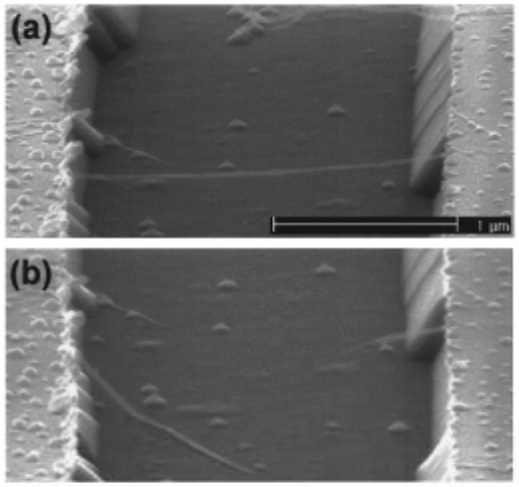

FIG. 2. Rope of single-wall nanotubes freely suspended over trench in silicon before (a) and after (b) being stressed past its elastic limit.

APPLIED PHYSICS LETTERS VOLUME 74, NUMBER 25 21 JUNE 1999

D. A. Walters,[a] L. M. Ericson, M. J. Casavant, J. Liu, D. T. Colbert, K. A. Smith, and R. E. Smalley

Nanoscopic investigations of the mechanical properties

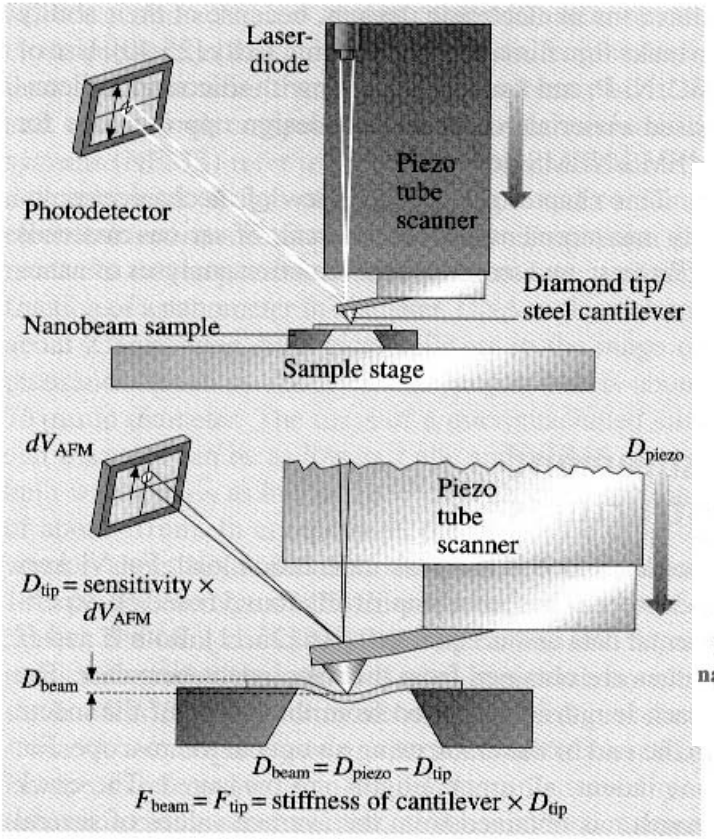

Fig. 25.1 Schematic showing the details of a nanoscale bending test. The AFM tip is brought to the center of the nanobeam and the piezo is extended over a known distance. By measuring the tip displacement, a load-displacement curve of the nanobeam can be obtained [25.38]

AFM can be used to apply local (and controlled) deformations

Stress/strain (and fracture) by AFM

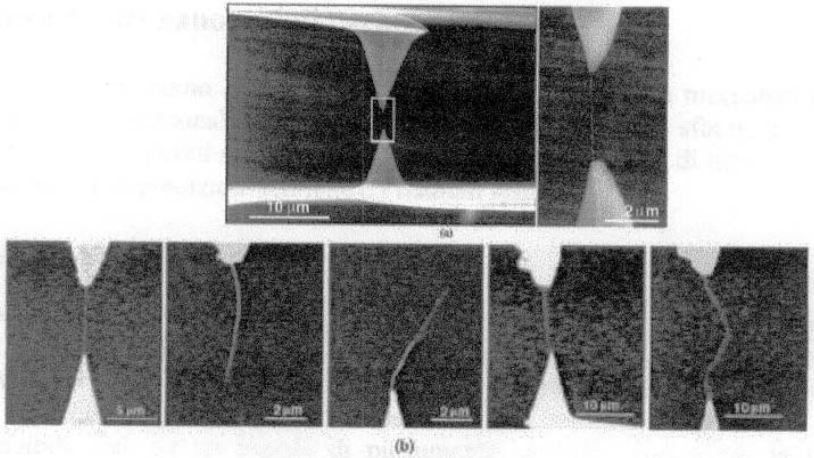

Figura 19 - Immagini SEM che mostrano (a) l'apparato per la misura di carico tensile di MWCNT con un nanotubo attaccato a due punte AFM opposte prima dell'imposizione del carico; (b) il meccanismo di frattura "telescopico" tipico dei MWCNTs.

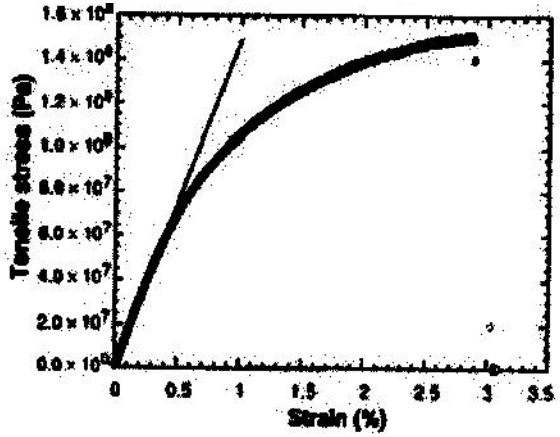

Figura 20 - Grafico stress-strain in misure tensili condotte su fibre di SWCNT.

A (very) few examples of AFM nanomechanics with CNTs I

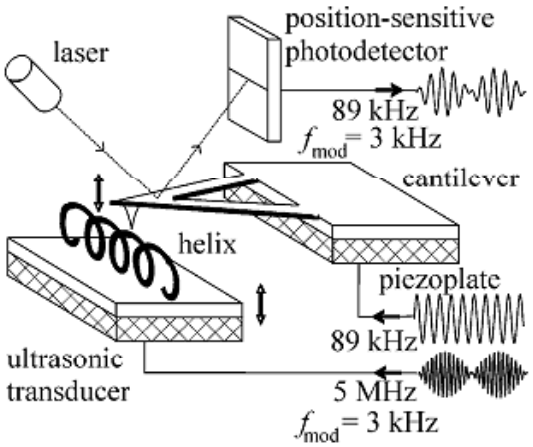

Fig. 1. Schematic view of our experimental set-up which allows the detection of mechanical resonances in a coiled nanotube using non-contact AFM

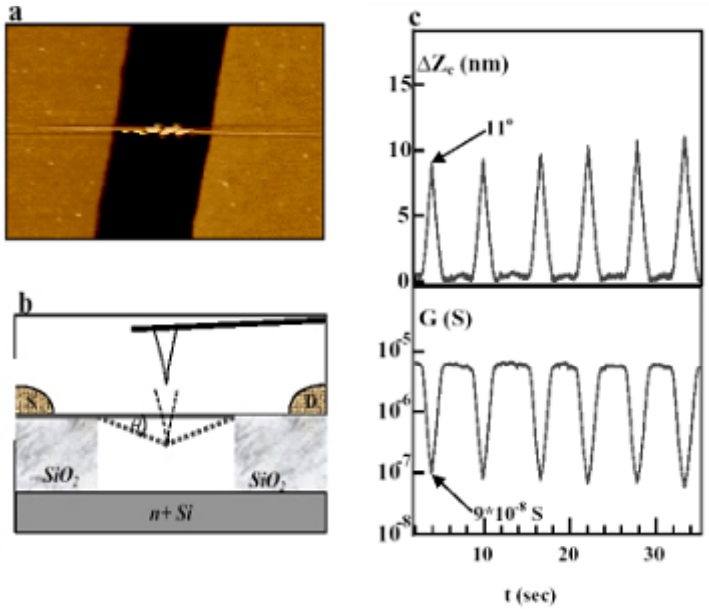

Fig. 5 Reversible conductance change induced by mechanical deformation of metallic nanotube using AFM tip. (a) AFM image of the nanotube on the trench. (b) Schematic illustration of the suspended nanotube and AFM tip induing the deformation. (c) Vertical displacement (ΔZ_C) and conductance (G) of nanotube during six reversible deformations with 6 sec interval.

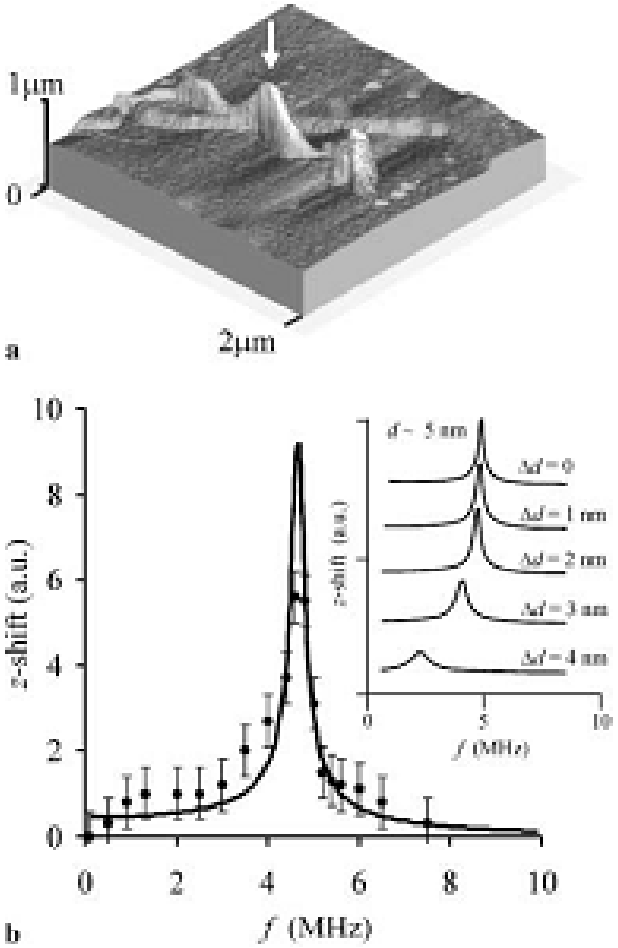

Fig. 2. a Three-dimensional non-contact AFM image of a suspended coiled nanotube bridging a step formed by the edge of a gold pad on a silicon substrate. b Vertical displacement of the AFM tip, which is positioned above the coiled nanotube (see white arrow in a), as a function of the excitation frequency. The *solid line* corresponds to a Lorentzian fit of the data. The *curves* in the inset correspond to the resonances measured during the stepped approach of the AFM tip towards the nanotube (step size Δd = 1nm)

A (very) few examples of AFM nanomechanics with CNTs II

VOLUME 84, NUMBER 24 PHYSICAL REVIEW LETTERS 12 JUNE 2000

Tensile Loading of Ropes of Single Wall Carbon Nanotubes and their Mechanical Properties

The mechanical response of 15 single wall carbon nanotube (SWCNT) ropes under tensile load was measured. For 8 of these ropes strain data were obtained and they broke at strain values of 5.3% or lower. The force-strain data are well fit by a model that assumes the load is carried by the SWCNTs on the perimeter of each rope. This model provides an average breaking strength of SWCNTs on the perimeter of each rope; the 15 values range from 13 to 52 GPa (mean 30 GPa). Based on the same model the 8 average Young's modulus values determined range from 320 to 1470 GPa (mean 1002 GPa).

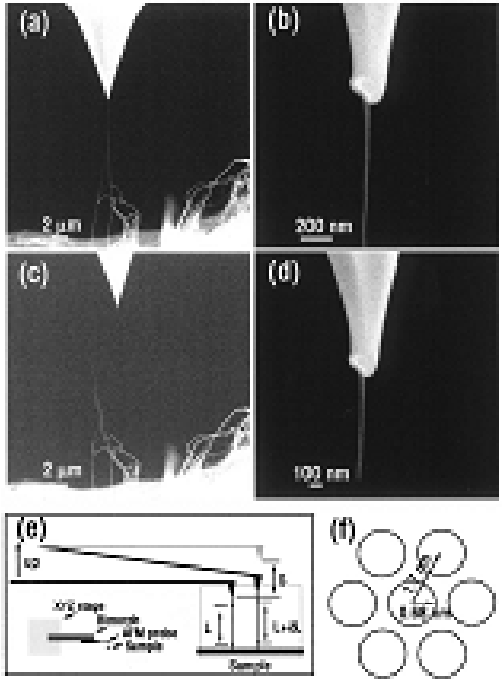

FIG. 1. SEM images showing a SWCNT rope tensile-loading experiment, before and after the SWCNT rope was broken. (a) A tensile loaded SWCNT rope between an AFM tip and a SWCNT "paper" sample. (b) Close-up view showing the attachment (carbonaceous deposit) of the end of the SWCNT rope to the AFM tip. (c) The same SWCNT rope after being loaded to the point where it broke. The image shows that one rope fragment was about 1 μm from the attachment region on the AFM tip. (d) Another close-up view of the attachment area after the rope was broken, showing the deposit was still robust. (e) A schematic showing an overview of the tensile-loading experiment. In the schematic, the gray cantilever indicates where the cantilever would be if no rope were attached on the AFM tip. (f) The assumed close-packed SWCNT rope with hexagonal cross section used in the paper for the purpose of calculating the cross-sectional area from the diameter measured with the SEM.

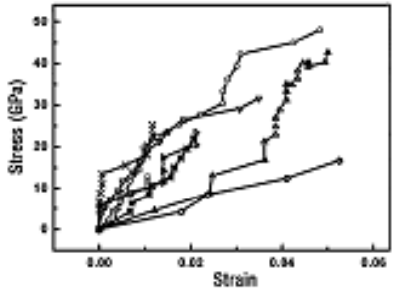

FIG. 2. Eight stress versus strain curves obtained from the tensile-loading experiments on individual SWCNT ropes. Each rope diameter is measured at high magnification (~100 000) in the SEM, accuracy a few nm. The stress values have been calculated using the cross-sectional area of the perimeter SWCNTs, according to the geometric model (see Fig. 1(f) and Ref. [25]). The SWCNT ropes for which strain could be determined were (see also Table I) C (□), D (○), E (△), G (▽), K (◇), M (▷), O (*), P (×).

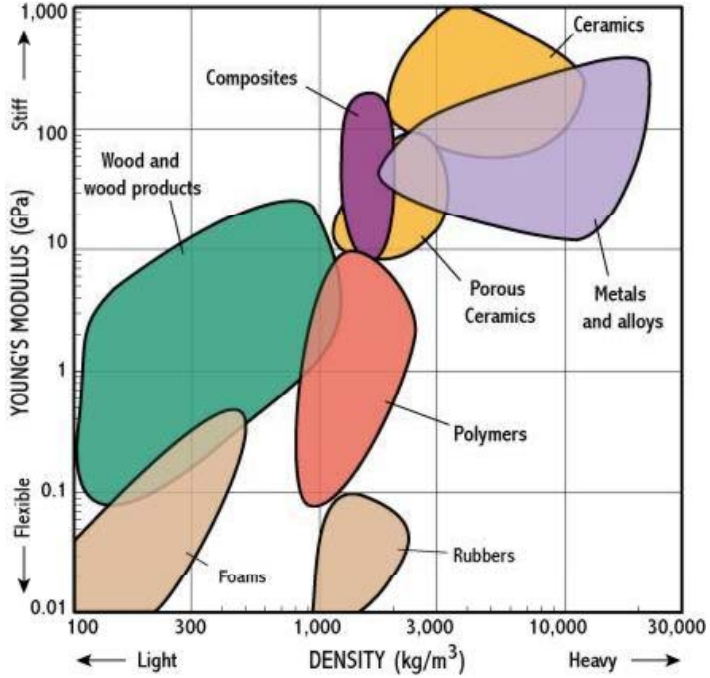

Conclusions

- The atomic force microscopy is based on probing mechanical interatcions at the very local scale
- The methods, the approach, the techniques, the technologies involved in AFM are (more or less) readily available for probing mechanical properties at the small and ultra-small scales
- Motivations oar associated with the need for analysis of nanosized samples or of locally inhomogeneous surfaces
- However, measurements suggest the occurrence of specific systems at the ultra-small scales with peculiar mechanical properties
- *A vivid example of the above is Carbon NanoTubes*